

Cite this: *Dalton Trans.*, 2024, **53**, 8202

Polymorph transformation in a mixed-stacking nickel-dithiolene complex with the derivative of 4,4'-bipyridinium†

Yan Gao,^a Lei Xu,^a Zi-Heng Feng,^a Yin Qian,^{id} *^a Zheng-Fang Tian^{id} ^b and Xiao-Ming Ren^{id} *^{a,c}

In this study, two polymorphs of the [1,1'-dibutyl-4,4'-bipyridinium][Ni(mnt)₂] salt (**1**) were synthesized. The dark-green polymorph (designated as **1-g**) was prepared under ambient conditions by the rapid precipitation method in aqueous solutions. Subsequently, the red polymorph (labeled as **1-r**) was obtained by subjecting **1-g** to ultrasonication in MeOH at room temperature. Microanalysis, infrared spectroscopy, thermogravimetry (TG), differential scanning calorimetry (DSC), and powder X-ray diffraction (PXRD) techniques were used to characterize the two polymorphs. Both **1-g** and **1-r** exhibit structural phase transitions: a reversible phase transition at ~403 K (~268 K) upon heating and 384 K (~252 K) upon cooling for **1-g** (**1-r**) within the temperature range below 473 K. Interestingly, on heating **1-r** to 523 K, an irreversible phase transition occurred at about 494 K, resulting in the conversion of **1-r** into **1-g**. Relative to **1-r**, **1-g** represents a thermodynamically metastable phase wherein numerous high-energy conformations in butyl chains of cations are confined within the lattice owing to quick precipitation or rapid annealing from higher temperatures. Through variable-temperature single crystal and powder X-ray diffractions, UV-visible spectroscopy, dielectric spectroscopy, and DSC analyses, this study delves into the mechanism underlying phase transitions for each polymorph and the manual transformation between **1-g** and **1-r** as well.

Received 2nd February 2024,
Accepted 16th April 2024

DOI: 10.1039/d4dt00324a

rsc.li/dalton

Introduction

Polymorphism is commonly observed in inorganic, organic (including small molecule and polymer crystals), and hybrid materials, representing the ability of a species to exist in distinct crystalline structures due to the differences in packing arrangements and molecular conformations. The different polymorphs often exhibit significant variations in their optical properties,^{1,2} conduction,^{3,4} magnetic behavior,^{5,6} hardness, color, solubility, hygroscopicity, filterability, and compactability.⁷

The transformation between polymorphs can be induced through temperature variations,⁸ high-pressure/strain tech-

niques,³ light irradiation,^{9,10} ion irradiation,¹¹ applied electric field,¹² and chemical treatments.^{3,13–17} These methods offer opportunities for the controlled preparation of anticipated polymorphs with desirable functionalities, fostering their practical applications.

Numerous planar metal-bis-dithiolene radical complexes have undergone extensive investigation to date because of their diverse magnetic and electric properties. These properties include metallic behavior,^{18–21} superconducting,²² Peierls²³/spin-Peierls transition,^{24,25} and charge-density wave^{22,26} characteristics. In particular, these radical complexes typically exhibit multiple polymorphic forms.^{4–6,27–29} Limited attention has been directed towards investigating planar bis-metal-dithiolene complexes with a closed-shell electron structure compared to their radical counterparts. This is primarily due to the absence of magnetic and electronic characteristics typically associated with the closed-shell electron structure of these complexes. Consequently, reports on polymorphic phenomena within this subset of complexes have been scarce.

Viologens, derivatives of 4,4'-bipyridinium, are a class of electron acceptors that typically exhibit three different oxidation states, 0, +1, and +2, corresponding to colorless, blue, and yellowish hues, respectively. They have found widespread

^aState Key Laboratory of Materials-Oriented Chemical Engineering and College of Chemistry and Molecular Engineering, Nanjing Tech University, Nanjing 211816, P. R. China. E-mail: yinqian@njtech.edu.cn, xmren@njtech.edu.cn

^bHubei Key Laboratory of Processing and Application of Catalytic Materials, Huanggang Normal University, Huanggang, 438000, P. R. China

^cState Key Laboratory of Coordination Chemistry, Nanjing University, Nanjing 210093, P. R. China

†Electronic supplementary information (ESI) available. CCDC 2311213 and 2311215. For ESI and crystallographic data in CIF or other electronic format see DOI: <https://doi.org/10.1039/d4dt00324a>

application in the preparation of electrochromic materials.^{30,31} On the contrary, bis-metal-dithiolene complex anions with closed-shell electron structures, such as $[\text{Ni}(\text{mnt})_2]^{2-}$ (mnt^{2-} = maleonitriledithiolate), serve as electron donors, with the $[\text{Ni}(\text{mnt})_2]^{2-}$ dianion potentially undergoing stepwise electron loss to attain various oxidation states such as -1 and 0 . Notably, the molecular cores of the 4,4'-bipyridinium dication and $[\text{Ni}(\text{mnt})_2]^{2-}$ dianion exhibit similar lengths and geometries. Accordingly, coulombic attractive interactions between the 4,4'-bipyridinium dication and $[\text{Ni}(\text{mnt})_2]^{2-}$ dianion favor the formation of an alternating mixed stack of anions and cations. This arrangement suggests the possibility of electron transfer occurring between the 4,4'-bipyridinium dication and $[\text{Ni}(\text{mnt})_2]^{2-}$ dianion within the mixed stack, potentially leading to novel optical, magnetic, or electronic properties.

In a prior investigation, we explored a planar nickel-bis-dithiolene salt, $[\text{C}_7\text{-}4,4'\text{-BiPy}][\text{Ni}(\text{mnt})_2]$ ($\text{C}_7\text{-}4,4'\text{-BiPy}^{2+}$ signifies 1,1'-diheptyl-4,4'-bi-pyridinium). Our study revealed two distinct crystal forms of $[\text{C}_7\text{-}4,4'\text{-BiPy}][\text{Ni}(\text{mnt})_2]$, among which a red-colored form is synthesized in an aqueous solution, while a dark-green polymorph is obtained by transforming the red microcrystals under ultrasound in MeOH at ambient conditions. Notably, this represents the initial instance of polymorphism observed in the $[\text{Ni}(\text{mnt})_2]^{2-}$ salt, marking a unique discovery.³² To broaden the scope of this investigation, considering the potential impact of alkyl chain lengths within 1,1'-dialkyl-4,4'-bipyridinium cations on the crystal packing, we

examined the crystal structure and dielectric properties of $[\text{C}_4\text{-}4,4'\text{-BiPy}][\text{Ni}(\text{mnt})_2]$ (**1**; $\text{C}_4\text{-}4,4'\text{-BiPy}^{2+}$ represents 1,1'-dibutyl-4,4'-bipyridinium). Our findings revealed that **1** exhibits two different crystalline forms, each undergoing a reversible phase transition. Consequently, we investigated deeply into the mechanisms governing these phase transitions and polymorphic transformations.

Results and discussion

Synthesis and characterization

The preparation and comprehensive characterization of **1** are detailed in the ESI.† Initially synthesized in an aqueous solution under ambient conditions, **1** underwent rapid precipitation, which was subsequently collected *via* filtration. Washing with water continued until the filtrate became colorless. The resulting precipitates were then transferred to an oven and dried at 40 °C for 4 hours, resulting in a dark-green sample (Fig. 1a, labeled as **1-g**). Subsequently, **1-g** underwent immersion in MeOH and was subjected to ultrasonic treatment for half hour, yielding a microcrystalline sample that appeared red in color (Fig. 1c, labeled as **1-r**). Interestingly, this situation contrasts with the observation made for $[\text{1,1'-diheptyl-4,4'-bipyridinium}][\text{Ni}(\text{mnt})_2]$. Initially formed as a red-colored precipitate in an aqueous solution, it later transformed into a green sample upon exposure to ultrasound in MeOH.³²

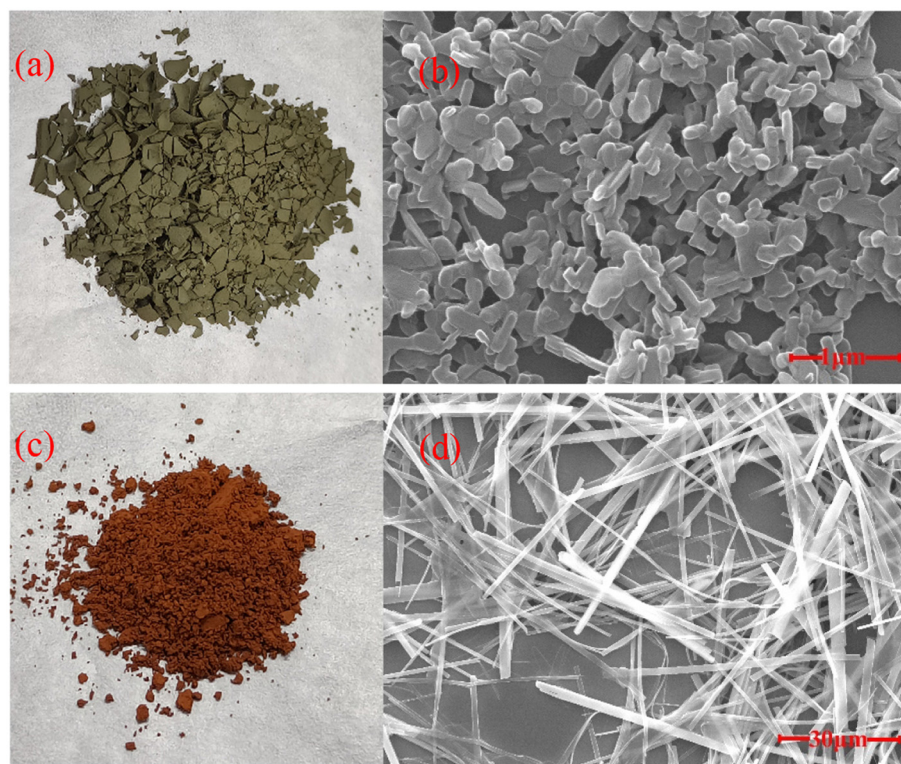


Fig. 1 Images of optical and SEM of **1**. (a and b) The sample of **1-g** quickly precipitated in the aqueous solution, and (c and d) this sample was ultrasonically treated in MeOH.

Comparative microanalysis of both **1-g** and **1-r** (ESI[†]) revealed relative C, H, and N element contents consistent with the calculated values for the formula C₂₆H₂₆N₆NiS₄, indicating identical chemical composition in both **1-g** and **1-r**, and both are two polymorphic forms of [C₄-4,4'-BiPy][Ni(mnt)₂].

In the realm of polymorphic transformations through chemical treatments, the mechanisms can be categorized into two subsets. These subsets involve solvent or adsorbent-induced solid-to-solid transformations and dissolved-recrystallization.¹⁴ Such forms are frequently observed in metal-organic frameworks (MOFs) or porous coordination polymers (PCPs). Typically, solvent or adsorbent molecules coordinate with the metal ions in the framework, resulting in alterations in the coordination geometry. These changes are pivotal in driving polymorphic transformations. For example, Kitagawa and colleagues identified that the synergistic interplay between adsorbent CO and available Cu²⁺ sites induce a comprehensive framework transformation within a soft nanoporous Cu²⁺-PCP crystal.¹⁵ The latter phenomenon has been found across multiple crystalline solid structures. Notably, Zang and coworkers observed a reversible solid-to-solid transformation within a two-dimensional Kagomé lattice porous coordination polymer (PCP-1) transitioning primarily to a distorted Kagomé intermediate (PCP-2). This was succeeded by an *in situ* dissolved-recrystallized process, resulting in the formation of a three-dimensional NbO framework (PCP-3).¹⁴ Typically, a polymorph possessing higher solubility tends to undergo solvent-mediated transformation, wherein it dissolves and subsequently recrystallizes into another polymorph characterized by lower solubility, while the differences in solubility between polymorphs stem from differences in lattice energy.⁷ The microcrystals of **1-g** show a limited solubility in MeOH, suggesting that the transformation from **1-g** to **1-r** involves a dissolution-recrystallization process and **1-g** shows lower lattice energy in comparison to **1-r**. Scanning electron microscopy (SEM) images depicted in Fig. 1b and d exhibit the morphological alteration between **1-g** and **1-r**, and **1-g** presents a characteristic flake-like morphology with a maximum size of *ca.* 0.3 μm. In contrast, **1-r** shows a belt-like shape with dimensions exceeding 30 μm, approximately two orders of magnitude larger than those observed in **1-g**.

The experimental PXRD patterns of **1-g** and **1-r**, along with the simulated one derived from single crystal diffraction data of **1-r**, are presented in Fig. 2a–c. Remarkably, the most intense diffraction peak in **1-g** shifts towards a smaller 2θ angle compared to that observed in **1-r**, indicating distinct crystalline structures between the two samples.

The IR spectra of **1-g** and **1-r** are displayed in Fig. 2d–g and Fig. S1,[†] respectively, with the corresponding characteristic vibration bands elucidated in Table 1. The characteristic vibrational bands associated with 1,1'-dioctyl-4,4'-bipyridinium concern two spectral regions. The ν_{C–H} bands in pyridyl rings and butyl chains are located at 3150–2850 cm⁻¹. In **1-g**, some of these bands exhibit a shift towards lower frequencies, while others demonstrate a movement towards higher frequencies compared to those observed in **1-r**. Additionally, the ν_{C=C}

bands within the pyridyl rings occur within the range of 1561–1439 cm⁻¹, displaying a slight redshift in **1-g** compared to that observed in **1-r**. The representative IR spectral bands from the anion primarily include the ν_{C=N}, ν_{C=C}, ν_{C–C} + ν_{C–S} and ν_{C–S} vibrations in mnt²⁻.³³ The most intensive band originating from the B_{2u} symmetry of ν_{C=N} in mnt²⁻ appears at 2196.7 cm⁻¹ for both **1-g** and **1-r**, indicating the characteristic of the dianion. In addition, the B_{3u} symmetry of the ν_{C=N} band as well as the ν_{C–C} + ν_{C–S} and ν_{C–S} bands in mnt²⁻ in **1-g** exhibit a slight redshift compared to those in **1-r**. However, the ν_{C=C} band in the mnt²⁻ of **1-g** shifts to a higher frequency compared to that in **1-r**. Theoretical analysis revealed that the highest occupied molecule orbital (MO) of the [Ni(mnt)₂]²⁻ dianion comprises the 3d_{xz} orbital of Ni²⁺ ion and the π orbital of mnt²⁻ ligands. This MO shows bonding characteristic for the C=C bond and antibonding characteristics for the C–S, C–C, Ni–S, and C≡N bonds. The anticipated transfer of electrons or negative charge from this MO to other acceptors is expected to result in a weakening of the C=C bond and a strengthening of the C–S, C–C, Ni–S, and C≡N bonds.^{33–35} The IR spectra illustrated lower frequencies for the vibrational bands of ν_{C–S}, ν_{C–C} and ν_{C=N} with lower frequencies, while the band of ν_{C=C} exhibited a higher frequency **1-g** compared with those in **1-r**. This observation demonstrates a lesser extent of charge transfer in **1-g** in comparison to **1-r**.

The solid-state UV-visible diffusion reflectance spectra in the 200–2500 nm region were collected under ambient conditions for **1-g** and **1-r**, as depicted in Fig. 3a. The curves of **1-g** and **1-r** exhibit an overlap in the spectral range of 200–500 nm, and the electron transition bands in this spectral region are attributed to π → π* within both an anion and a cation as well as MLCT charge-transfer bands within an anion. Additionally, the absorption bands in the spectral range of 500–800 nm are relevant to d–d transitions of Ni²⁺ ions and MLCT charge-transfer transitions within an anion. Furthermore, ion-pair charge transfer (IPCT) occurs from the anionic HOMO to the cationic LUMO. Comparatively, the electron transition bands arising from the d–d transitions of Ni²⁺ ions and MLCT charge-transfer transitions within an anion are contrasted with the IPCT transition band, which is rather sensitive to the packing arrangement of anions and cations in the crystal structure.^{36,37} However, a noticeable difference emerges in the spectral region in the range of 500–2500 nm, and the differences in the visible light spectrum between 500–800 nm result in distinct polymorphs with differing colors. TG plots of **1-g** and **1-r**, as shown in Fig. 3b, demonstrate similar weight loss behavior; moreover, they indicate that both polymorphs are thermally stable up to approximately 550 K.

Single crystal structures of **1-r**

Given that **1-g** is exclusively obtained through the initial synthesis in an aqueous solution, rapid precipitation impedes the attainment of sufficiently large single crystals necessary for single-crystal X-ray diffraction analysis. Consequently, in this study, only the crystal structures of **1-r** were determined. DSC measurements unveiled a thermal anomaly occurring at about

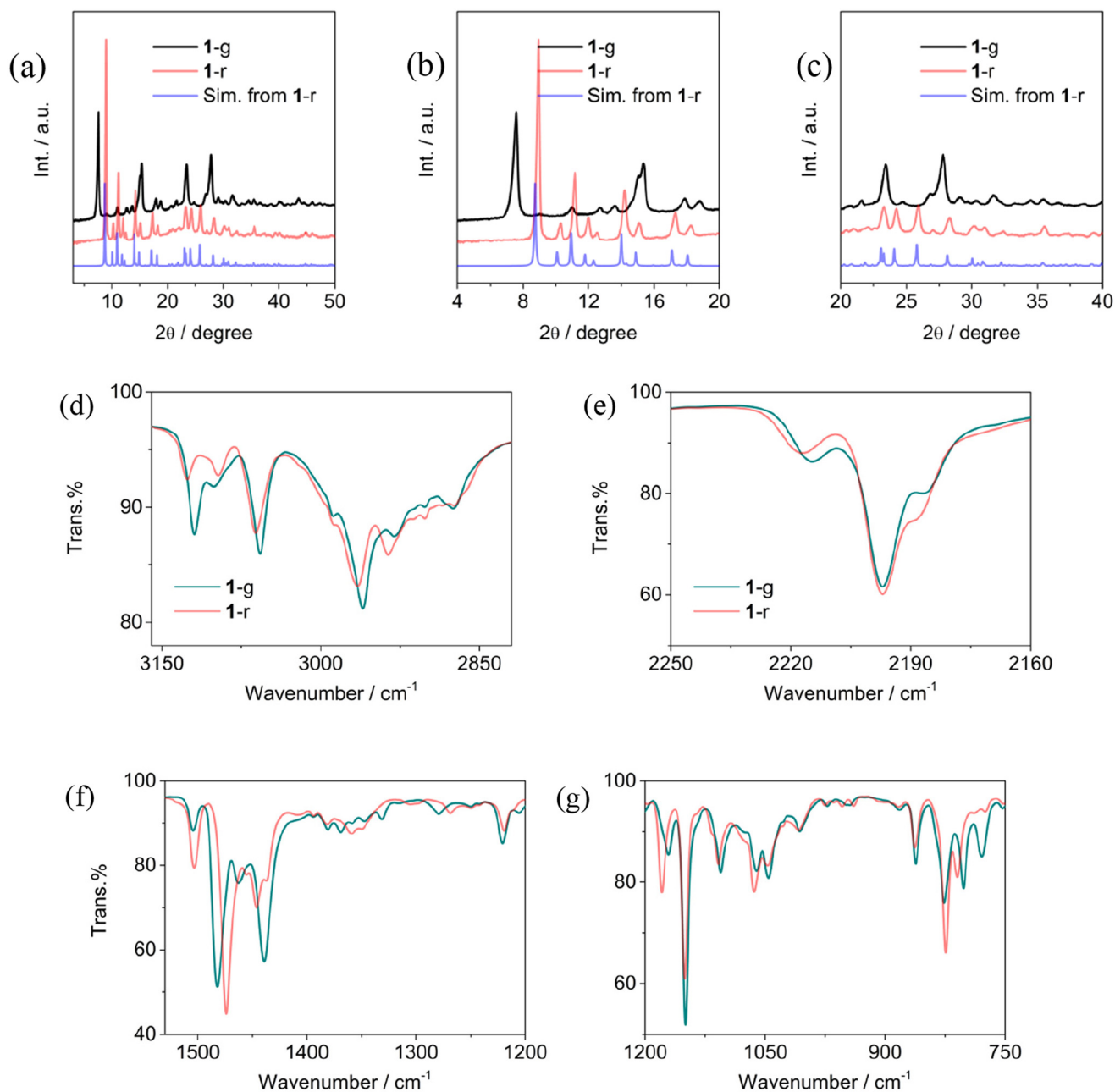


Fig. 2 (a–c) PXRD patterns of **1-g** and **1-r**, in which the black and red lines represent the experimental PXRD patterns of **1-g** and **1-r**, and the blue line is the simulated one obtained from the single crystal data of **1-r**. (d–g) IR spectra of **1-g** and **1-r** in different frequency regions.

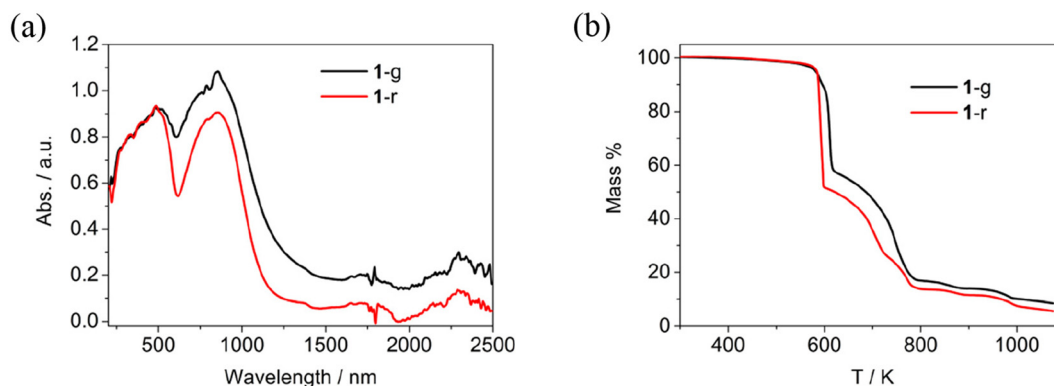
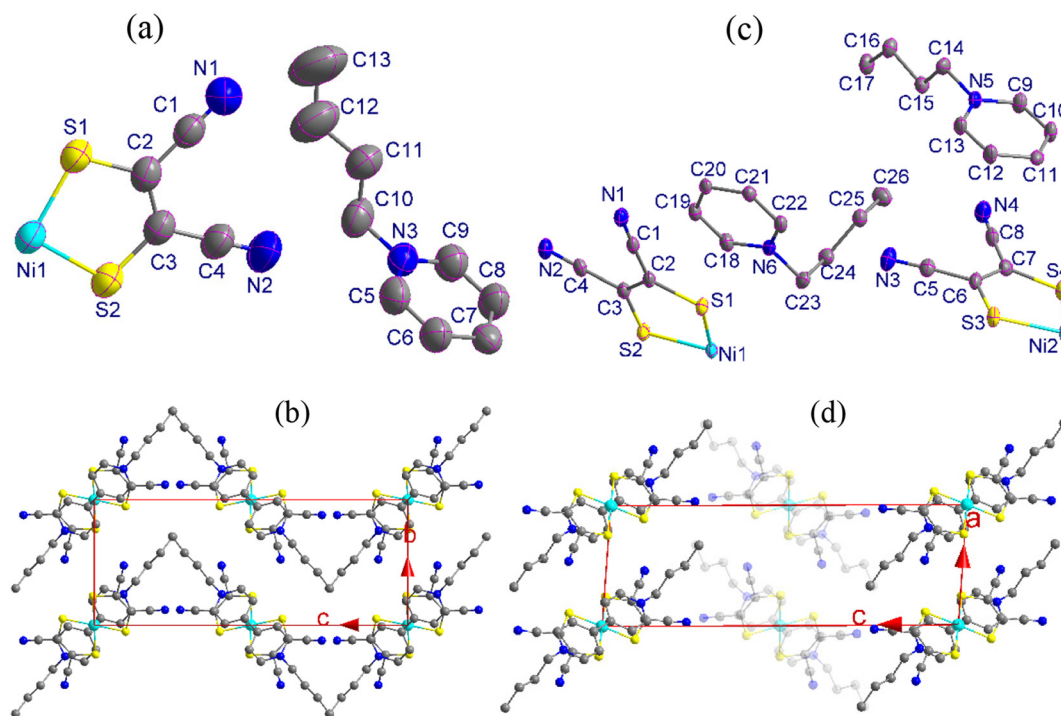
268 K for **1-r** (refer to the next section of DSC investigation). As a result, the crystal structures of **1-r** were investigated both below (low-temperature phase, abbreviated as LTP) and above (high-temperature phase, abbreviated as HTP) this critical temperature of 268 K.

The crystal structure of **1-r** crystallizes in the monoclinic system with space group $P2_1/c$ at 296 K, and the crystal data and structure refinement parameters in HTP are summarized in Table S1.† Its asymmetric unit comprises one-half $[\text{Ni}(\text{mnt})_2]^{2-}$ paired with one-half $\text{C}_4\text{-}4,4'\text{-Bipy}^{2+}$ (Fig. 4a). Both the anion and the cation possess an inversion center, which is located at the

Ni^{2+} ion within the planar $[\text{Ni}(\text{mnt})_2]^{2-}$ and the midpoint of the C7–C7#1 bond (#1 = $1 - x, 1 - y, -z$) in $\text{C}_4\text{-}4,4'\text{-Bipy}^{2+}$, respectively. The two pyridyl rings adopt a coplanar manner, while the butyl chain shows a fully *trans*-conformation, tilted towards the pyridyl rings, resulting in a chair-shaped conformation within $\text{C}_4\text{-}4,4'\text{-Bipy}^{2+}$. Bond lengths and angles within both the cation and the anion adhere to standard ranges.^{32,38,39} The anions (A) and the cations (C) are arranged in a mixed-stacking fashion of ...CACA... along the *a*-axis direction (Fig. 4b), with identical distances of Ni in the anion to the midpoint of the C7–C7#1 bond in the cation within a mixed-stacking column. The mixed-stack-

Table 1 Comparison of the typical vibrational bands in IR spectra of 1-g and 1-r

Band in 1-g (cm ⁻¹)	Band in 1-r (cm ⁻¹)	Assignment ³³
3119.4 s, 3101.5 m, 3057.7 s	3127.0 m, 3096.5 m, 3063.0 s	ν_{C-H} in pyridyl ring
2987.6 sh, 2960.8 s, 2930.5 s, 2902.3 w, 2875.2 m	2987.3 sh, 2964.7 s, 2936.0 s, 2901.9 w, 2873.7 sh	ν_{C-H} in butyl chain
2215.2 m, 2196.7 vs, 2186.2 sh	2217.3 m, 2196.7 vs, 2188.1 sh	$\nu_{C=N}$ in mnt ²⁻
1557.5 s, 1504.4 s, 1463.1 s, 1439.1 vs	1560.5 s, 1504.3 s, 1446.6 s	$\nu_{C=C}/\nu_{C=N}$ in pyridyl ring
1482.5 vs	1473.6 vs	$\nu_{C=C}$ in mnt ²⁻
1170.9 s	1179.3 s	$\nu_{C-C} + \nu_{C-S}$ in mnt ²⁻
861.8 s	863.4 s	ν_{C-S} in mnt ²⁻

**Fig. 3** (a) Solid-state UV-visible spectra and (b) TG plots of 1-g and 1-r.**Fig. 4** ORTEP views of 1-r with thermal ellipsoids at a 50% probability level (H atoms omitted) for the crystal structures at (a) 296 K and (c) 100 K. The comparatively packing arrangements in the crystal structures at (b) 293 K and (d) 100 K for 1-r.

ing columns show the same orientation along the *b*-axis direction, while they show wave-shape arrangement along the *c*-axis direction (Fig. 4b). Such a type of alignment is distinct from that observed in other [1,1'-di-*R*-4,4'-BiPy][M(mnt)₂] (herein, M = Ni,

Cu, Pd or Pt; 1,1'-di-*R*-4,4'-BiPy²⁺ is the cation of 1,1'-dialkyl-4,4'-bipyridinium, 1,1'-diphenyl-4,4'-bipyridinium or 1,1'-dibenzyl-4,4'-bipyridinium).^{32,38-42} The mean-molecule planes of [Ni(mnt)₂]²⁻, defined by the NiS₄ core in the anion, and the two

coplanar pyridyl rings in the cation, display nearly parallel stacking with a $3.03(1)^\circ$ dihedral angle within a mixed-stacking column. The mean-molecule planes of $[\text{Ni}(\text{mnt})_2]^{2-}$ make a dihedral angle of $57.83(2)^\circ$ between the neighboring mixed-stacking columns along the *c*-axis direction (Fig. 4b and Fig. S2†).

Upon transition from the HTP to the LTP, the space group of **1-r** undergoes a transformation from monoclinic $P2/c$ to triclinic $P\bar{1}$ (the crystal data and structure refinement parameters in LTP are summarized in Table S1†), and the asymmetric unit doubles compared to that observed in HTP, comprising of two halves of $[\text{Ni}(\text{mnt})_2]^{2-}$ anions (two crystallographically distinct Ni^{2+} ions are denoted as Ni1 and Ni2, respectively) along with two halves of $\text{C}_4\text{-}4,4'\text{-Bipy}^{2+}$ cations; the distinction between two crystallographically inequivalent cations is determined by the nitrogen atoms on their respective pyridyl rings, namely, N5 and N6, as depicted in Fig. 4c. The butyl chains exhibit a fully *trans*-conformation in the cation containing N5, resembling that observed in HTP. Conversely, a *gauche* conformation is observed between C23 and C24 in the cation containing N6 (Fig. S3 and S4†). As a result, the phase transition occurring at about 268 K during heating in **1-g** is attributed to the thermally-induced conformational changes in the butyl chains within certain $\text{C}_4\text{-}4,4'\text{-Bipy}^{2+}$ cations.

Although the packing arrangements in both the HTP and LTP exhibit similarities, the equivalent mixed-stacking columns in the HTP undergo subdivision into two distinct

entities. One type involves anions with Ni1 and cations containing N6, forming a set of regular mixed-stacking columns, while the other comprises anions with Ni2 and cations containing N5, establishing a separate set of regular mixed-stacking columns, illustrated as semitransparent columns in Fig. 4d. The mean-molecule planes of $[\text{Ni}(\text{mnt})_2]^{2-}$ and the two pyridyl rings in the cation display a dihedral angle of $5.45(6)^\circ/6.75(6)^\circ$ in the mixed-stacking columns containing Ni1/Ni2. Notably, these angles are approximately twice as large as those observed in the HTP. The mean-molecule planes of $[\text{Ni}(\text{mnt})_2]^{2-}$ between the anions containing Ni1 and Ni2 exhibit a dihedral angle of $61.19(2)^\circ$, indicating a slight increase compared to that observed in the HTP.

Phase transition and thermal triggering polymorphic transformation

DSC analyses were conducted below 473 K with two heating-cooling cycles for both **1-g** and **1-r** (Fig. 5a and b), and the variations of enthalpy and entropy, together with the peak temperatures of thermal anomalies, are summarized in Table S2† for each phase transition observed in **1-g** and **1-r**. Two polymorphs showed reversible thermal anomalies, with peak temperatures recorded at 403/384 K for **1-g** and 268/252 K for **1-r** during the heating/cooling cycles (Fig. 5a and b). The single crystal structure analysis for **1-r** and the variable-temperature PXRD pattern investigation for **1-g** (Fig. S5†) revealed a struc-

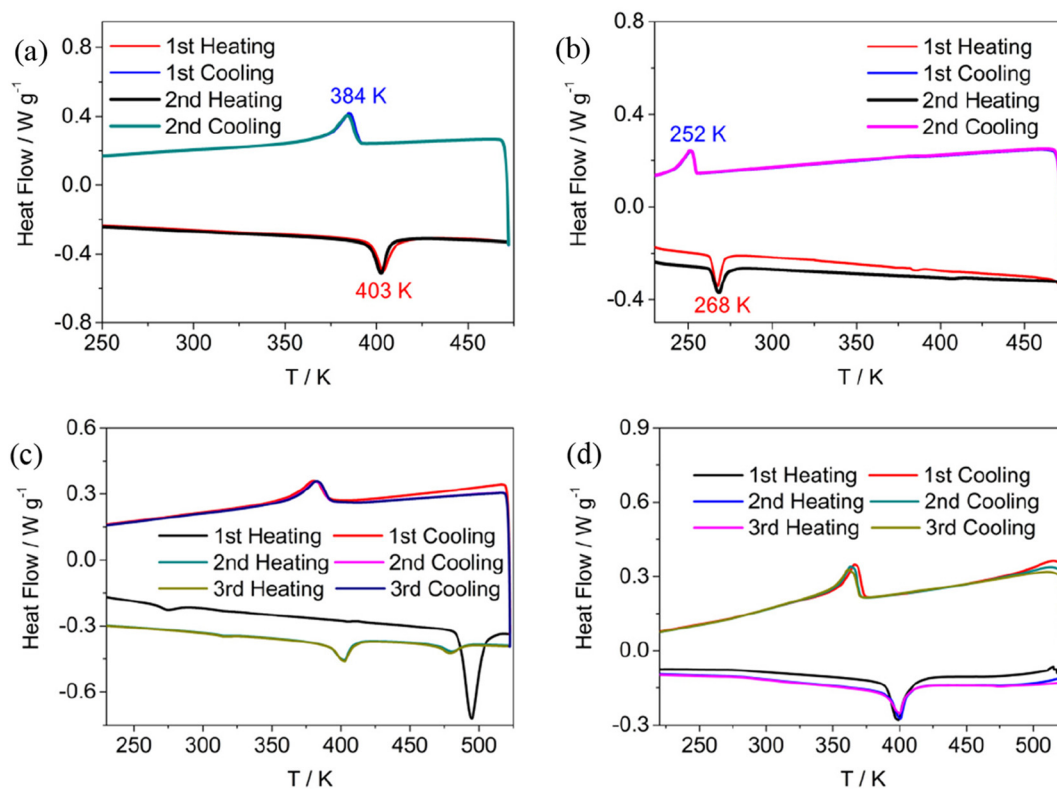


Fig. 5 DSC plots of (a) **1-g** and (b) **1-r** at the temperatures below 473 K with two heating-cooling cycles; (c) **1-r** and (d) **1-g** at the temperatures below 523 K with three heating-cooling cycles.

tural phase transition corresponding to the observed thermal anomaly. For description convenience, the phases of 1-g below and above 403/384 K upon heating/cooling are named as its LTP/HTP. An intriguing irreversible thermal anomaly emerges at about 494 K upon heating 1-r to 523 K (Fig. 5c); furthermore, the thermal anomaly observed at 268/252 K in the initial heating process disappears, replaced by two endothermic peaks at *ca.* 402 K and 480 K, together with an exothermic peak at *ca.* 382 K over the subsequent two continuous heating-cooling cycles (the changes of enthalpy and entropy are listed in Table S2† for each phase transition). The proximity of the endothermic and exothermic peaks at 402 K and 382 K to the critical temperatures in 1-g is noteworthy. In addition, the endothermic peak at 480 K is close to the critical temperature of 495 K observed upon the initial heating. No new thermal anomalies manifest in the DSC plot of 1-g upon heating it to 523 K (Fig. 5d).

The annealing of 1-r was performed at temperatures of 423 K, 473 K, and 523 K, respectively, with their corresponding PXRD patterns presented in Fig. 6a. The PXRD pattern resulting from the annealing at 423 K mirrors that of the pristine sample of 1-r. Contrastingly, the PXRD pattern obtained at 473 K illustrates the presence of the phases of both 1-r and 1-g, while the pattern from the annealing at 523 K corresponds to that of 1-g. This alignment between the PXRD patterns and

their association with specific annealing temperatures resonates with the findings observed in DSC measurements. Variable-temperature PXRD measurements were conducted for 1-r, as depicted in Fig. 6b. The findings reveal that at 473 K, 1-r initiates a partial transformation towards 1-g, with the complete polymorphic transition occurring at 523 K. It is noteworthy that the PXRD patterns of 1-r exhibit a high degree of similarity at 523 K and after annealing back to 298 K. However, it is evident that all the diffraction peaks at 523 K shift towards smaller 2θ angles compared to those observed at 298 K. This discrepancy is attributed to thermal expansion.

Fig. 6c illustrates the variable-temperature PXRD patterns of the 1-g sample. The PXRD profiles of the pristine sample at 298 K and its annealed counterpart at 523 K, subsequently cooled back to 298 K, demonstrate significant similarity. The distinct differences that appear in the PXRD patterns are observed at 450 K and 523 K, temperatures surpassing the thermal anomaly threshold (403 K during heating). A noticeable shift is observed in the diffraction peak at the smallest 2θ angle, indicating a movement towards lower values. Moreover, the PXRD patterns at 450 K and 523 K exhibit similarity to each other but differ from the pristine sample at 298 K. This observation strongly suggests a reversible structural phase transition in 1-g occurring at about 403/384 K during the heating/cooling process.

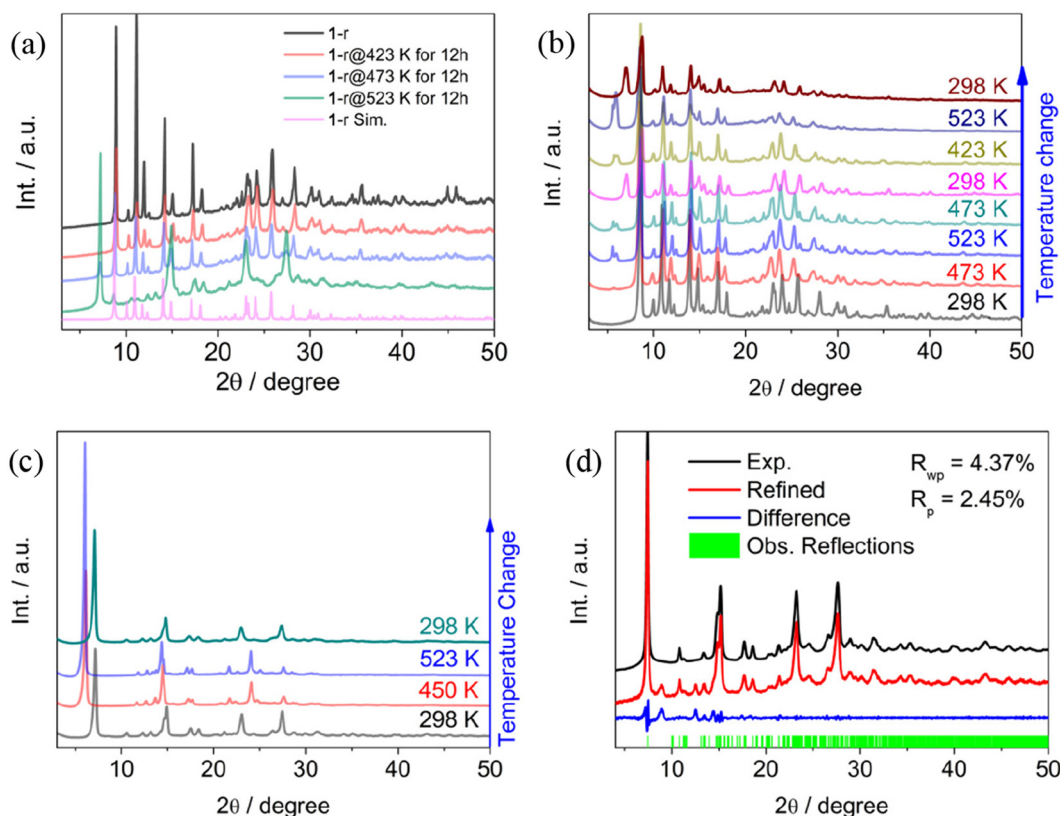


Fig. 6 (a) PXRD patterns of 1-r annealed at different temperatures together with the simulated PXRD pattern of 1-r at room temperature, (b) variable-temperature PXRD patterns of 1-r with thermal cycles from 298 K → 473 K → 523 K → 473 K → 298 K → 423 K → 523 K → 298 K, (c) variable-temperature PXRD patterns of 1-g with thermal cycles from 298 K → 473 K → 523 K → 298 K, and (d) experimental and refined PXRD patterns of 1-g.

Polymorph **1-r** exhibits a transformation into **1-g** upon annealing at temperatures exceeding 473 K. This transformation demonstrates that both polymorphs share a similar packing arrangement of anions and cations within their respective crystal structures. The diffraction data of **1-g** at room temperature underwent Pawley refinement using the Reflex module within Materials Studio. The refinement process used the crystal structure of **1-r** at 296 K as the initial model structure and involved the removal of background signals from the PXRD pattern of **1-g**. The refinement results suggest that **1-g** at room temperature likely exhibits monoclinic symmetry within the *P2* space group, with unit cell parameters of $a = 9.1276 \text{ \AA}$, $b = 8.3632 \text{ \AA}$, $c = 24.3659 \text{ \AA}$; $\beta = 98.89^\circ$. The obtained R_{wp} value is 4.37%, and R_p stands at 2.45%. Fig. 6d displays the experimental PXRD pattern of **1-g** at room temperature alongside its refined counterpart, from which the background has been removed. Both patterns, experimental and refined, demonstrate a strong match, corroborating their alignment. From the single crystal structure analysis of **1-r**, the diffraction peak at $2\theta = 8.975^\circ$ in the PXRD pattern of **1-r** at room temperature corresponds to the $[0\ 0\ 1]$ crystal orientation. The expansion of the lattice along the $[0\ 0\ 1]$ crystal orientation signifies an increase in the distance between adjacent mixed-stacking columns. Building upon the aforementioned analysis, the metastable nature of **1-g** compared to the thermodynamically stable **1-r** suggests the probable presence of high-energy conformations in the butyl chains of the cations, such as the *gauche* conformation. Alkyl chain conformational polymorphism has been observed in polymer poly(vinylidene fluoride), which is renowned for its five distinct conformational polymorphs (namely, α , β , γ , δ , and ϵ forms). Across these polymorphs, the chains of poly(vinylidene fluoride) run parallel to each other, yet the conformation of the chains varies distinctly. The most thermodynamically stable phase, β -phase, characterized by an all-*trans* conformation, exhibits the shortest interchain distance at 8.58 Å. Alternately, the interchain distances in other phases range between 9.64 and 9.66 Å.⁴³ Integration of findings from literature³⁶ and crystal structure analysis of **1-r** at room temperature leads to the conclusion that repulsive interactions between butyl chains in *gauche* conformations contribute to an expansion in distances between adjacent mixed-stacking columns.

The concept of entropy is related to the level of disorder within a system. Further analysis of entropy changes during phase transitions and polymorphic transformations were conducted using the equation $\Delta S = R \ln(N_2/N_1)$. Here, R represents the gas constant valued at $8.314 \text{ J mol}^{-1} \text{ K}^{-1}$, while N_1 and N_2 denote the microscopic state numbers in phase-1 and phase-2, respectively. In the context of an order-disorder phase transition, the ratio N_2/N_1 approximately corresponds to the ratio of orientation numbers among disordered molecules or ions. The N_2/N_1 ratio is estimated at ~ 1.5 and 56.9 during the phase transition of **1-r** at temperatures of about $\sim 274 \text{ K}$ and $\sim 495 \text{ K}$ upon initial heating, respectively. It stands at ~ 10.4 during the phase transition of **1-g** at $\sim 404 \text{ K}$ upon initial heating. These findings demonstrate a significant prevalence of disordered

conformations within the butyl chains of the cations during the transformation from **1-r** to **1-g** as well as during the transition from LTP to HTP of **1-g**.

The microcrystals of **1-g** exhibit a dark-green color in LTP, transitioning to a dark red color in HTP. This color variation corresponds to changes in the absorption spectrum within the visible light range (Fig. S6†). Importantly, this process of color alternation is reversible, indicating that **1-g** displays reversible thermochromism. Conversely, the microcrystals of **1-r** display a red color at room temperature. As the temperature increases to 423 K, the color shifts to dark red. After being elevated to 523 K, **1-r** retains its dark red coloration, which transitions back towards that resembling **1-g** upon cooling down to 298 K, also showing thermochromism in **1-r** (Fig. S7 and S8†). The color change with temperature is in agreement with the variation in the UV-visible optical spectra of **1-g** and **1-r** (Fig. 7).

Mechanically inducing polymorphic transformation

The microcrystals of **1-g** were ground for 5 minutes under ambient conditions, resulting in a color change from dark-green to earthy red, as depicted in the set of Fig. 8a. The analysis of the UV-visible spectra of both the pristine and ground samples of **1-g** reveals that piezochromism is associated with spectral variations in the 550–800 nm range (Fig. 8a). Furthermore, a comparison of PXRD patterns indicates that the ground sample of **1-g** exhibits the characteristic diffractions of **1-r**, suggesting a transformation of part of the **1-g** sample into **1-r** during the grinding process (Fig. 8b).

Dielectric property

Fig. 9a and b illustrate the graphs depicting the real part of dielectric permittivity (ϵ') against temperature during the initial heating and cooling cycles at the selected frequencies. Fig. 9c shows the $\epsilon'-T$ plots at a frequency of 10^5 Hz across two heating-cooling cycles for **1-r** within the temperature range of 200–473 K. The ϵ' values range from 12.5 to 13.0 at temperatures below 340 K and exhibit minimal dependence on frequency, however, they display thermally-activated dielectric relaxation behavior at temperatures above 340 K. A knee-shaped anomaly emerges at *ca.* 268 K in the $\epsilon'-T$ plots during the initial heating process, consistent with the thermal anomaly temperature observed in the DSC plot of **1-r** (refer Fig. 5b). Both the thermal and the dielectric anomalies are attributed to the structural phase transition. During the initial cooling and the subsequent reheating, knee-shaped anomalies manifest at *ca.* 397 K and 408 K, respectively. Subsequently, the dielectric anomaly persists at about 397 K in the subsequent cooling process. The observed dielectric anomaly temperatures of 397 K and 408 K during the second cooling and heating processes closely align with the respective thermal anomaly temperatures for **1-g**. However, the earlier observed dielectric anomaly at about 268 K during the initial heating process is no longer present.

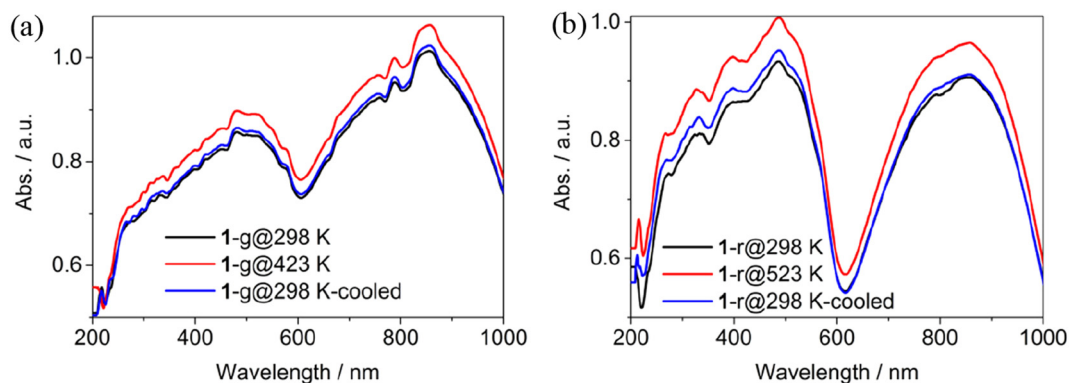


Fig. 7 Variable-temperature solid UV-visible-near IR absorbed spectra of (a) 1-g and (b) 1-r.

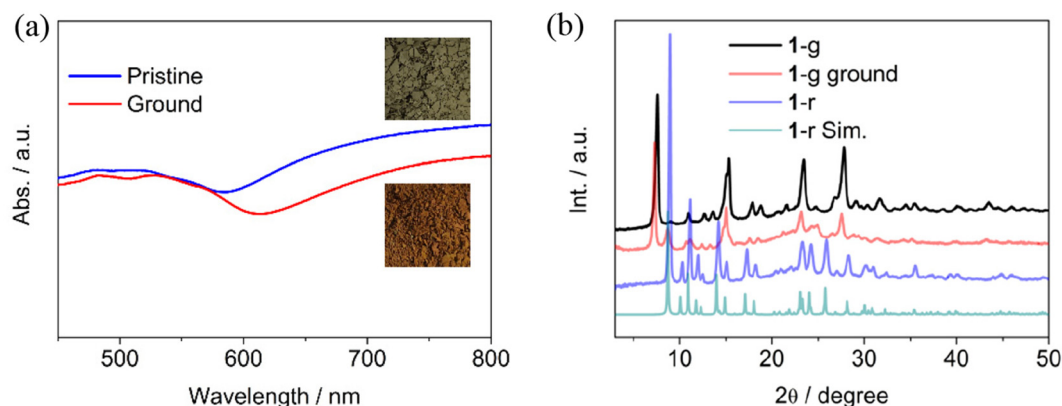


Fig. 8 Solid visible spectra of 1-g: (a) pristine and ground for 5 minutes (the inset: images of pristine and ground 1-g), and (b) PXRD patterns of 1-g, 1-g ground for 5 minutes and 1-r.

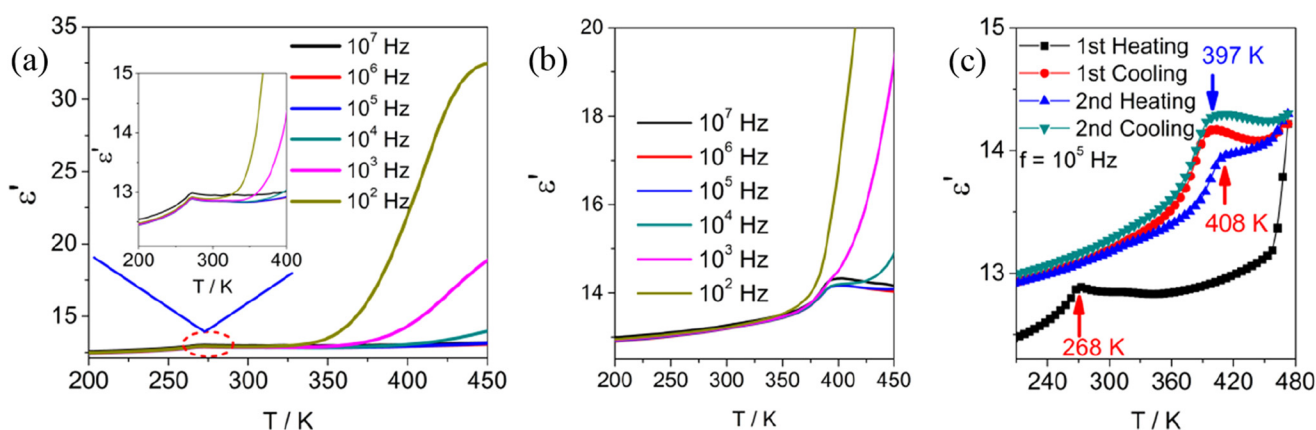


Fig. 9 Plots of the real part of dielectric permittivity (ϵ') versus temperature at the selected frequencies in 200–450 K for 1-r: (a) the inset showing the anomaly at about 268 K, and the anomaly at about 397 K in the initial heating run. (b) The anomaly at about 397 K in the initial cooling. (c) Plots of ϵ' - T at the frequency of 10^5 Hz with two heating-cooling cycles for 1-r, showing a dielectric anomaly at about 268 K during the initial heating process, consistent with the thermal anomaly temperature observed in the DSC plot of 1-r (refer Fig. 5b).

Mutual transformation between two polymorphs

Through the analysis of DSC, variable-temperature PXRD patterns, UV-visible reflection and dielectric spectra of both 1-g

and 1-r, and the Pawley refinement of PXRD pattern of 1-g at room temperature, the conclusion is drawn that 1-r and 1-g represent the thermodynamically stable and kinetically favorable polymorphic forms of $[C_4-4,4'-BiPy][Ni(mnt)_2]$, respect-

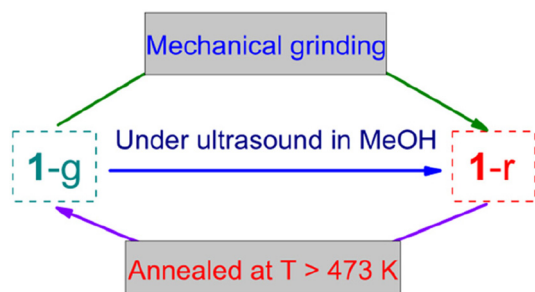


Fig. 10 Schematic illustration of the mutual transformation between 1-g and 1-r.

ively. The structural disparity between 1-g and 1-r mainly concerns the separations between the adjacent mixed-stacking columns, which are more extensive in 1-g compared to 1-r. The mutual transformation between 1-g and 1-r is depicted schematically in Fig. 10.

Conclusion

In this study, two polymorphs of the [1,1'-dibutyl-4,4'-bipyridinium][Ni(mnt)₂] salt were obtained. Aqueous solutions containing 1,1'-dibutyl-4,4'-bipyridinium and [Ni(mnt)₂]²⁻ ions were mixed at ambient conditions, resulting in the formation of a dark-green solid labeled as 1-g. This solid was subjected to ultrasonic treatment in MeOH, leading to the transformation into a red solid denoted as 1-r. The transition from 1-g to 1-r in MeOH involves dissolution and subsequent recrystallization. Furthermore, mechanical grinding also facilitates the conversion of 1-g into 1-r. Two polymorphs exhibit structural phase transitions: 1-g (1-r) undergoes a reversible phase transition at about 403 K (268 K) upon heating and 384 K (252 K) upon cooling within the temperature range below 473 K. However, upon heating 1-r to 523 K, an irreversible thermal anomaly emerges at about 494 K, leading to the transformation of 1-r into 1-g. In contrast to 1-r, 1-g represents a thermodynamically metastable polymorph wherein multiple high-energy conformations of butyl chains are trapped within the lattice due to rapid precipitation or quick annealing from elevated temperatures. The immobilized high-energy conformations of the butyl chains can be altered to lower-energy states through mechanical grinding or heating, resulting in piezochromism and thermochromism.

Conflicts of interest

There are no conflicts to declare.

Acknowledgements

This work was financially supported by Priority Academic Program Development of Jiangsu Higher Education

Institutions, Jiangsu Province, China; National Natural Science Foundation of China (Grant No. 22073047).

References

- 1 M. Mutailipu, M. Zhang, H. Wu, Z. Yang, Y. Shen, J. Sun and S. Pan, Ba₃Mg₃(BO₃)₃F₃ polymorphs with reversible phase transition and high performances as ultraviolet non-linear optical materials, *Nat. Commun.*, 2018, **9**, 3089.
- 2 Q. Benito, X. F. Le Goff, S. Maron, A. Fargues, C. Martineau, F. Taulelle, S. Kahlal, T. Gacoin, J.-P. Boilot and S. Perruchas, Polymorphic copper iodide clusters: insights into the mechanochromic luminescence properties, *J. Am. Chem. Soc.*, 2014, **136**, 11311–11320.
- 3 H. Yang, S. W. Kim, M. Chhowalla and Y. H. Lee, Structural and quantum-state phase transitions in van der Waals layered materials, *Nat. Phys.*, 2017, **13**, 931–937.
- 4 T. Akutagawa, H. Koshinaka, Q. Ye, S. Noro, J. Kawamata, H. Yamaki and T. Nakamura, Conformational polymorph of o-aminoanilinium(dibenzo[18]crown-6) supramolecules in [Ni(dmit)₂]⁻ salts, *Chem. – Asian J.*, 2010, **5**, 520–529.
- 5 H. B. Duan, X. R. Chen, H. Yang, X. M. Ren, F. Xuan and S. M. Zhou, Disorder-order transformation and significant dislocation motion cooperating with a surprisingly large hysteretic magnetic transition in a nickel-bisdithiolene spin system, *Inorg. Chem.*, 2013, **52**, 3870–3877.
- 6 X. R. Chen, W. H. Ning, H. Yang, J. L. Liu, F. Xuan and X. M. Ren, Observation of hysteretic magnetic phase transitions coupled with orientation motion of ions and dielectric relaxation in a one-dimensional nickel-bis-dithiolene molecule solid, *Dalton Trans.*, 2014, **43**, 6251–6261.
- 7 L. Nicoud, F. Licordari and A. S. Myerson, Estimation of the solubility of metastable polymorphs: a critical review, *Cryst. Growth Des.*, 2018, **18**, 7228–7237.
- 8 X. Zheng, C. Wu, S. K. Jha, Z. Li, K. Zhu and S. Priya, Improved phase stability of formamidinium lead triiodide perovskite by strain relaxation, *ACS Energy Lett.*, 2016, **1**, 1014–1020.
- 9 K. A. Deresz, R. Kamiński, S. E. Kutniewska, A. Króczyński, D. Schaniel and K. N. Jarzemska, An optically reversible room-temperature solid-state cobalt(III) photoswitch based on nitro-to-nitrito linkage isomerism, *Chem. Commun.*, 2022, **58**, 13439–13442.
- 10 Z. Lin, M. C. Folgueras, H. K. D. Le, M. Gao and P. Yang, Laser-accelerated phase transformation in cesium lead iodide perovskite, *Matter*, 2022, **5**, 1455–1465.
- 11 A. Azarov, C. Bazioti, V. Venkatachalapathy, P. Vajeeston, E. Monakhov and A. Kuznetsov, Disorder-induced ordering in gallium oxide polymorphs, *Phys. Rev. Lett.*, 2022, **128**, 015704.
- 12 C. Mart, T. Kämpfe, K. Kühnel, M. Czernohorsky, S. Kolodinski, M. Wiatr, W. Weinreich and L. M. Eng, Enhanced pyroelectric response at morphotropic and field-induced phase transitions in ferroelectric hafnium oxide thin films, *APL Mater.*, 2021, **9**, 051120.

- 13 M. M. Zhao, L. Meng, Y. Y. Xu, N. Du and F. Yen, Inducing ferroelectricity in NH_4I and NH_4Br via partial replacement of protons by deuterons, *J. Phys. Chem. C*, 2023, **127**, 20951–20955.
- 14 L. H. Cao, Y. S. Wei, H. Xu, S. Q. Zang and T. C. W. Mak, Unveiling the mechanism of water-triggered diplex transformation and correlating the changes in structures and separation properties, *Adv. Funct. Mater.*, 2015, **25**, 6448–6457.
- 15 H. Sato, W. Kosaka, R. Matsuda, A. Hori, Y. Hijikata, R. V. Belosludov, S. Sakaki, M. Takata and S. Kitagawa, Self-accelerating CO sorption in a soft nanoporous crystal, *Science*, 2014, **343**, 167–170.
- 16 M. E. Sun, Y. Li, X. Y. Dong and S. Q. Zang, Thermoinduced structural-transformation and thermochromic luminescence in organic manganese chloride crystals, *Chem. Sci.*, 2019, **10**, 3836–3839.
- 17 S. K. Ghosh, W. Kaneko, D. Kiriya, M. Ohba and S. Kitagawa, A bistable porous coordination polymer with a bond-switching mechanism showing reversible structural and functional transformations, *Angew. Chem., Int. Ed.*, 2008, **47**, 8843–8847.
- 18 N. Tenn, N. Bellec, O. Jeannin, L. Piekara-Sady, P. Auban-Senzier, J. Iniguez, E. Canadell and D. Lorcy, A single-component molecular metal based on a thiazole dithiolate gold complex, *J. Am. Chem. Soc.*, 2009, **131**, 16961–16967.
- 19 Y. Kosaka, H. M. Yamamoto, A. Nakao, M. Tamura and R. Kato, Coexistence of conducting and magnetic electrons based on molecular π -electrons in the supramolecular conductor (Me-3,5-DIP)[Ni(dmit)₂]₂, *J. Am. Chem. Soc.*, 2007, **129**, 3054–3055.
- 20 A. Kobayashi, T. Naito and H. Kobayashi, Low-temperature crystal and band electronic structures of metallic M(dmit)₂ (M = Ni, Pd) compound, *Synth. Met.*, 1995, **70**, 1047–1048.
- 21 H. Tanaka, Y. Okano, H. Kobayashi, W. Suzuki and A. Kobayashi, A three-dimensional synthetic metallic crystal composed of single-component molecules, *Science*, 2001, **291**, 285–287.
- 22 W. Kaddour, P. Auban-Senzier, H. Raffy, M. Monteverde, J.-P. Pouget, C. R. Pasquier, P. Alemany, E. Canadell and L. Valade, Charge density wave and metallic state coexistence in the multiband conductor TTF[Ni(dmit)₂]₂, *Phys. Rev. B: Condens. Matter Mater. Phys.*, 2014, **90**, 205132.
- 23 M. M. Ahmad, D. J. Turner, A. E. Underhill, C. S. Jacobsen, K. Mortensen and K. Carneiro, Physical properties and the Peierls instability of $\text{Li}_{0.82}[\text{Pt}(\text{S}_2\text{C}_2(\text{CN})_2)_2] \cdot 2\text{H}_2\text{O}$, *Phys. Rev. B: Condens. Matter Mater. Phys.*, 1984, **29**, 4796–4799.
- 24 M. Tamura, A. Nakao and R. Kato, Frustration-induced valence-bond ordering in a new quantum triangular antiferromagnet based on [Pd(dmit)₂], *J. Phys. Soc. Jpn.*, 2006, **75**, 093701.
- 25 H. B. Duan, X. M. Ren and Q. J. Meng, One-dimensional (1D) [Ni(mnt)₂][−]-based spin-Peierls-like complexes: Structural, magnetic and transition properties, *Coord. Chem. Rev.*, 2010, **254**, 1509–1522.
- 26 L. Brossard, E. Canadell, L. Valadec and P. Cassoux, Weak electron correlations and charge-density waves in TTF[M(dmit)₂]₂, with M = Ni, Pd, *Synth. Met.*, 1995, **70**, 1045–1046.
- 27 M. L. Afonso, R. A. L. Silva, M. Matos, E. B. Lopes, J. T. Coutinho, L. C. J. Pereira, R. T. Henriques and M. Almeida, Growth of (Perylene)₂[Pd(mnt)₂] crystals, *J. Cryst. Growth*, 2012, **340**, 56–60.
- 28 Q. Ye, T. Akutagawa, N. Hoshino, T. Kikuchi, S. Noro, R. G. Xiong and T. Nakamura, Polymorphs and structural phase transition of [Ni(dmit)₂][−] crystals induced by flexible (trans-Cyclohexane-1,4-diammonium)(Benzo[18]crown-6)₂ supramolecule, *Cryst. Growth Des.*, 2011, **11**, 4175–4182.
- 29 S. Q. Zang, X. M. Ren, Y. Su, Y. Song, W. J. Tong, Z. P. Ni, H. H. Zhao, S. Gao and Q. J. Meng, Observation of magnetic bistability in polymorphs of the [Ni(dmit)₂][−] complexes, *Inorg. Chem.*, 2009, **48**, 9623–9630.
- 30 Y. Gu, W. Hong, W. Choi, J. Y. Park, K. B. Kim, N. Lee and Y. Seo, Electrochromic device containing heptyl viologen, PEDOT, TiO₂ and TEMPO, *J. Electrochem. Soc.*, 2014, **161**, H716–H721.
- 31 K. W. Shah, S. X. Wang, D. X. Y. Soo and J. Xu, Viologen-based electrochromic materials: from small molecules, polymers and composites to their applications, *Polymers*, 2019, **11**, 1839.
- 32 L. Xu, Y. M. Wang, Z. H. Feng, Y. Qian, Y. Gao, Z. F. Tian and X. M. Ren, Thermochromism of rapid response to temperature change versus mechanochromism in a Ni-dithiolene complex salt, *Dalton Trans.*, 2023, **52**, 8918–8926.
- 33 C. W. Schlapfer and K. Nakamoto, Infrared spectra and normal-coordinate analysis of 1,2-dithiolate complexes with nickel, *Inorg. Chem.*, 1975, **14**, 1338–1344.
- 34 G. N. Schrauzer and V. P. Mayweg, Coordination compounds with delocalized ground states. bisdithioglyoxalnickel and related complexes, *J. Am. Chem. Soc.*, 1965, **87**, 3585–3592.
- 35 A. T. Coomber, D. Beljonne, R. H. Friend, J. L. Brédas, A. Charlton, N. Robertson, A. E. Underhill, M. Kurmoo and P. Day, Intermolecular interactions in the molecular ferromagnetic $\text{NH}_4\text{Ni}(\text{mnt})_2 \cdot \text{H}_2\text{O}$, *Nature*, 1996, **380**, 144–146.
- 36 V. Madhu and S. K. Das, Near-IR absorption due to supramolecular electronic interaction in an extended 3D hydrogen-bonding network material: synthesis, crystal structure and properties of [4,4′-H₂bpy][Cu(mnt)₂], *Polyhedron*, 2004, **23**, 1235–1242.
- 37 B. Q. Yao, J. S. Sun, Z. F. Tian, X. M. Ren, D. W. Gu, L. J. Shen and J. Xie, Ion-pair charge transfer complexes with intense near IR absorption: Syntheses, crystal structures, electronic spectra and DFT calculations, *Polyhedron*, 2008, **27**, 2833–2844.
- 38 H. Kisch, A. Fernandez, Y. Wakatsuki and H. Yamazaki, Charge transfer complexes of nickel dithiolenes with methyl viologen, *Z. Naturforsch., B: J. Chem. Sci.*, 1985, **40**, 292–297.

- 39 Y. Chen, S. P. Zhao, J. L. Liu, W. H. Ning, X. M. Sun and X. M. Ren, A bis(maleonitriledithiolato)nickelate charge-transfer salt with mixed stacks exhibiting novel non-ferroelectric-type dielectric phase transition and bistability, *RSC Adv.*, 2014, **4**, 9178–9181.
- 40 M. Lemke, F. Knoch and H. Kisch, Structure of the ion-pair charge-transfer complex (Methylviologen)²⁺[Pd(mnt)₂]²⁻, *Acta Crystallogr., Sect. C: Cryst. Struct. Commun.*, 1993, **49**, 1630.
- 41 F. Knoch, U. Ammon and H. Kisch, Crystal structure of *N,N'*-dimethyl-2,2'-bipyridinium bis(cis-1,2-dicyanoethene-1,2-dithiolato)platinate(II), ((CH₃)₂C₅NH₄C₅NH₄(CH₃))(Pt(S₂C₂(CN)₂)₂), *Z. Kristallogr.*, 1995, **210**, 77–78.
- 42 T. Mochida, Y. Funasako, T. Kishida and C. Kachi-Terajima, Assembled structures and magnetic properties of viologen-[M(mnt)₂] charge-transfer salts (mnt²⁻ = maleonitriledithiolate; M = Cu, Ni, Pt), *Inorg. Chim. Acta*, 2012, **384**, 111–116.
- 43 Z. Cui, N. T. Hassankiadeh, Y. Zhuang, E. Drioli and Y. M. Lee, Crystalline polymorphism in poly(vinylidene-fluoride) membranes, *Prog. Polym. Sci.*, 2015, **51**, 94–126.